ChemSusChem
Full Papers

DOI: 10.1002/cssc.201((will be completed by the editorial staff))

# Graphene Oxide (GO)/α-$Bi_2O_3$ Versatile Multifunctional Composites for Enhanced Visible Light Photocatalysis, Chemical Catalysis and Solar Energy Conversion

Tirtha Som,*[a] Gerald V. Troppenz,[b] Robert Wendt, [a,c] Markus Wollgarten[c] Jörg Rappich,[b] Franziska Emmerling,[d] Klaus Rademann[a]

[a] *Dr. T. Som, R. Wendt, Prof. Dr. K. Rademann*
*Institut für Chemie*
*Humboldt-Universität zu Berlin*
*Brook-Taylor-Strasse 2, 12489 Berlin (Germany)*
*E-mail: tirthasom@gmail.com*

[b] *G. V. Troppenz, Dr. J. Rappich*
*Institut für Silizium-Photovoltaik*
*Helmholtz-Zentrum Berlin für Materialien und Energie GmbH*
*Kekuléstrasse 5, 12489 Berlin (Germany)*

[c] *R. Wendt, Dr. M. Wollgarten*

*Helmholtz-Zentrum Berlin für Materialien und Energie GmbH*

*Hahn-Meitner-Platz 1, 14109 Berlin (Germany)*

[d] *Dr. F. Emmerling*
*BAM Bundesanstalt für Materialforschung und -prüfung*
*Richard-Willstätter-Strasse 11, 12489 Berlin (Germany)*

*Supporting information for this article is available on the WWW under http://dx.doi.org/10.1002/cssc.20xxxxxxx.*

*Dedicated to Prof. Dr. Drs. h.c. Helmut Schwarz on the occasion of his 70th birthday*

The growing challenges of environmental purification by solar photocatalysis, precious metal free catalysis and photocurrent generation in photovoltaic cells are receiving the utmost global attention. Here we demonstrate the one-pot green chemical synthesis of a new stable heterostructured, eco-friendly, multifunctional micro-composite consisting of α-$Bi_2O_3$ micro-needles intercalated with anchored graphene oxide (GO) micro-sheets (1.0 wt%) for the above mentioned applications in a large economical scale. The bare α-$Bi_2O_3$ micro-needles display twice as better photocatalytic activities than commercial $TiO_2$ (Degussa-P25) while the GO hybridized composite exhibit ~4-6 times enhanced photocatalytic activities than neat $TiO_2$ photocatalyst in the degradation of colored aromatic organic dyes (crystal violet and rhodamine 6G) under visible light irradiation (300 W tungsten lamp). The highly efficient activity is associated with the strong surface adsorption ability of GO for aromatic dye molecules, the high carrier acceptability and efficient electron-hole pair separation in $Bi_2O_3$ by individual adjoining GO sheets. Introduction of Ag nanoparticles (2.0 wt%) further enhances the photocatalytic performance of the composite over 8 folds due to a plasmon-induced electron-transfer process from Ag nanoparticles via GO sheets into the conduction band of $Bi_2O_3$. The new composites are also catalytically active. They catalyze the reduction of 4-nitrophenol to 4-aminophenol in presence of borohydride ions. Photoanodes assembled from GO/α-$Bi_2O_3$ and Ag/GO/α-$Bi_2O_3$ composites display an improved photocurrent response (power conversion efficiency ~ 20% higher) over those prepared without GO in dye-sensitized solar cells (DSSCs).

## Introduction

The fabrication of graphene and graphene-oxide (GO) incorporated novel hybrid materials, such as graphene oxide/semiconductor (GO/SC) composites, are being intensively pursued in recent years, due to their promising sustainable applications in environment conservation, [1-4] catalysis,[5,6] eco-fuel hydrogen generation,[7-9] and light energy harvesting.[10-12] Special focus is given to comprehend (i) the unique ability or the mechanistic pathway followed by these materials to photo-degrade carcinogenic and mutagenic aromatic industrial effluents[13,14] and other organic substances,[15] (ii) their role in

surface catalysis,[16,17] and (iii) contribution towards enhancing the existing photovoltaic cell efficiencies.[18]

GO structurally constitutes of the graphene framework with some oxygen containing functional groups. [19-21] The hydroxyl and epoxide groups are covalently bonded at the basal planes while the phenolic-OH and carboxylic groups are attached at the edges of the hexagonal carbon framework. [21-23] Depending on the preparation method, the C:O:H ratio in GO may range from 8:2:3 to 8:4:5. [24]

There are several physico-chemical advantages which GO possesses over reduced graphene oxide (RGO) that render GO to be a particularly suitable material for several applications, primarily in photocatalysis, catalysis, opto-electronics and electrochemistry. [19-24] The ionisable functional groups present on GO, act as binding sites facilitating the deposition and anchoring of nano-semiconductors, metal nanoparticles (NPs) and organic (dye) molecules via direct non-covalent, covalent, π–π and/or van der Waals interaction. [21-23,25] GO also offers an incredibly large surface area adsorption owing to the two accessible (exposed) sites which is often unavailable in coagulated RGO sheets due to van der Waals interaction between the reduced sheets. The Brunauer-Emmett-Teller (BET) surface area reported for RGO is about ~ 400-470 $m^2 g^{-1}$ [19] while the BET surface area reported for GO are in range ~ 600-900 $m^2 g^{-1}$. [26]

Graphene or RGO is a zero band gap material. In GO, the C-atoms that are covalently attached to the functional groups are $sp^3$ hybridized. These can be envisaged as locally oxidized regions disrupting the extended $sp^2$-conjugated honeycomb network. The $sp^2$-C fraction in GO is usually ~ 40% and these can be visualized as the unoxidized regions. [25-28] Upon reduction (thermal and chemical), the $sp^2$-C fraction can be increased to ~ 80% and the C/O ratio can be improved to approximately 12:1 with the loss of O-functional groups and restoration of conductive network.[19,23] Moreover, regulation of the $sp^2/sp^3$ carbon proportions in GO enables a continuous tuning of its band-gap from about 3.5 eV down to 1 eV.[27,28] This provide the opportunity to effectively align the position of the energy levels of GO (valance band) with respect to a variety of available semiconductors in a composite photocatalytic material. This facilitate effective charge transfer (electrons and holes) required to drive the photo-chemical or photo-electrochemical processes. Besides, GO also has excellent electron accommodating and shuttling ability. When combined with the SC, GO facilitates immediate charge separation and migration of the photo-excited SC. This GO effectively counteracts the high electron-hole pair recombination rate in bare SC and is expected to enhance the participation of electrons and holes in photo-driven processes.

A recent study by Kamat et al [29] demonstrates that GO anchored on $TiO_2$ can capture photogenerated electrons from the $TiO_2$. The electrons are transferred via a hopping mechanism to the other side of the GO and can reduce attached $Ag^+$ ions to Ag NPs.[29] GO is also known to effectively facilitate the electron transfer of several heme proteins. [30] GO can function both as p- and n-type materials (electron and hole extraction and transport material) depending on (i) the dopant introduced, [13,22] (ii) degree of oxidation (band gap), [21,22,31,32] and (iii) appropriate functionalization (charge neutralization). [11,20, 33,34]. This property of GO also promises its application as electrode material.[35-38] The field-effect mobilities in GO range between 2-200 $cm^2V^{-1}s^{-1}$ for holes and 0.5-30 $cm^2V^{-1}s^{-1}$ for electrons at room temperature. [39]

With the recent emphasis given to visible light (45% of sunlight) driven photocatalysis, Bi-containing oxides such as such as $Bi_2O_2CO_3$, $Bi_2WO_6$, $Bi_2MoO_6$, $BiVO_4$, BiOX (X = Br, I), $BiFeO_3$, $Bi_2Ti_2O_7$ and $Bi_2Sn_2O_7$ have wedged the attention due to their appealing optical and electronic properties. [30-46] $Bi_2O_3$ in particular, have emerged as one of the strongest contenders of the most popular UV-active $TiO_2$ photocatalyst.[47] Bismuth is non-toxic in its oxide forms and finds active applications as piezoelectric material,[48] biosensors,[49] functional glasses, etc. The investigation available on the photocatalytic activities of different phases of $Bi_2O_3$ [50,51] demonstrates their non-toxicity and resistance against photocorrosion. In combinations with noble metal NPs like Au-loaded α-$Bi_2O_3$ [52,53] and Ag-loaded β-$Bi_2O_3$,[54] the activity is seen to improve. Very recently, the first fabrication of a $Bi_2O_3$-based plasmonic photocatalyst (Pt/α-$Bi_2O_3$) has been reported.[55]

Plasmonic photocatalyst exploits the opto-electronic properties of both the plasmonic metal NPs and the semiconductor. The interesting light absorption properties of plasmonic photocatalysts in manipulating visible radiation have been subjects of numerous recent investigations. In the plasmonic photocatalysts, the noble metal NPs, such as Ag and Au, which exhibit surface plasmon resonance (SPR) absorption band around 410 and 520 nm respectively, (i) undergo plasmonic excitation in presence of visible light and injects the plasmonic electrons into the suitably located conduction band of the semiconductor. [56-60] The holes generated on the metal surface participate in dye degradation. (ii) The local electric field generated in the immediate vicinity of the metal NPs upon excitation at well-defined wavelengths enhance the rate of inherent electron–hole pair formation on the semiconductor surface and suppresses electron–hole recombination which can now participate in the oxidation-reduction processes. [56-60] (iii) The heat produced by the light absorbing plasmonic NPs further promotes the oxidation of organic pollutants. [56-60]

To the best of our literature survey, there is only one recent report of graphene – $Bi_2O_3$ composite as an electrode material for supercapacitors. [61] We therefore consider it important to undertake the green chemical synthesis of the new composites: GO/α-$Bi_2O_3$ and Ag/GO/α-$Bi_2O_3$ and explore their versatile applications in dye degradation, light energy conversion and catalysis. We also attempt to provide here a detailed insight on the mechanism of organic dye mineralization considering positions of the relative energy levels of the components in these heterostructured composites, enhanced catalysis and underlying response of improved photocurrent. Two recent feature articles by Tu et al[2] on the versatility of graphene-semiconductor nanocomposites and by Chen and Caruso [62] on the diverse applications of semiconductor architectures, motivates us further to undertake this multidimentional investigation of these new materials

## Results and Discussion

### Surface Morphology

The size and morphology of the synthesized photocatalysts is determined by scanning electron microscopy (SEM) and shown in **Figure 1**.

The α-$Bi_2O_3$ (**Figure 1a**) is seen to have a needle-like morphology. The morphology of the Ag NPs loaded α-$Bi_2O_3$ (Ag/$Bi_2O_3$) (**Figure 1b**) is very similar. The length of the needles ranges from 5 to 25 µm and the diameter is typically about 1 µm. The SEM images of the GO hybridized α-$Bi_2O_3$ (GO/$Bi_2O_3$) (**Figures 1c-d**) composite clearly show randomly oriented $Bi_2O_3$ needles intercalated with transparent GO sheets. The GO sheets are highlighted (in green) to emphasize their explicit intercalation and defined dimensions. The SEM images of the Ag NPs loaded GO hybridized α-$Bi_2O_3$ (Ag/GO/$Bi_2O_3$) (**Figures 1e-f**) are analogous to that of GO/$Bi_2O_3$. The original images corresponding to **Figures 1(c-f)** are shown in the supplementary as **Figures S1(a-d)**.

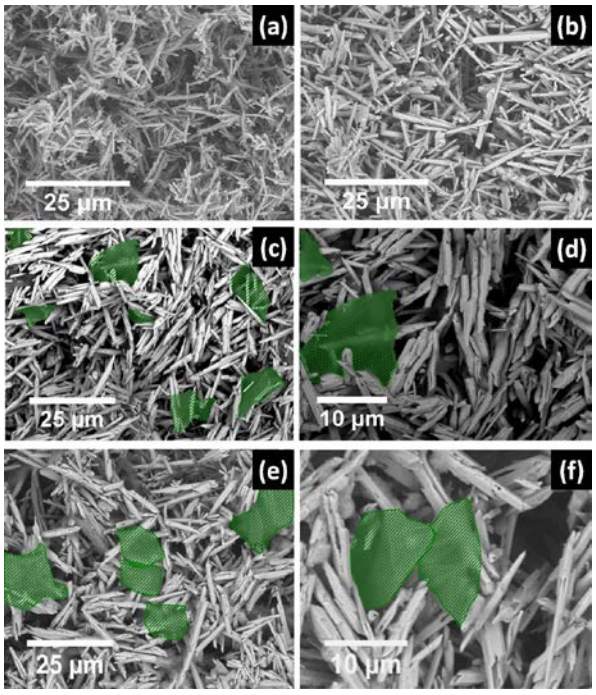


**Figure 1.** SEM images of (a) α-$Bi_2O_3$ needles, (b) Ag-uploaded α-$Bi_2O_3$ needles, (c) GO/$Bi_2O_3$, (d) GO/$Bi_2O_3$ at a higher magnification, (e) Ag/GO/$Bi_2O_3$ and (f) Ag/GO/$Bi_2O_3$ at a higher magnification. The intercalated GO sheets are highlighted in green color.

### Microscopic Morphology

The microscopic morphologies and structures of the Ag/GO/$Bi_2O_3$ sample are further investigated by transmission electron microscopy (TEM) to investigate~~observe~~ the presence of Ag NPs. In **Figure 2a**, an extended edge of a $Bi_2O_3$ needle is seen with dispersed Ag NPs near it and on its surface. In **Figures 2(b-d)** near-spherical Ag NPs are clearly seen to lie on the $Bi_2O_3$ needle surface. In **Figure 2e**, Ag NPs anchored on crumbled GO sheets are~~is~~ evident while **Figure 2f** further emphasizes the presence of near-spherical NPs. The size of the Ag NPs is found to vary widely from about 2 – 65 nm (supplementary **Figure S2**). The electron cloud (free conduction electrons) of the Ag NPs of this size range is expected to exhibit collective electronic oscillations relative to the positive metal core induced by an interacting electromagnetic field (SPR). The successful incorporation of plasmonic Ag and its involvement in electron donation to GO and $Bi_2O_3$ can be proven by monitoring GOs phonon modes i.e. by Raman backscattering experiments (**Figure 4**).

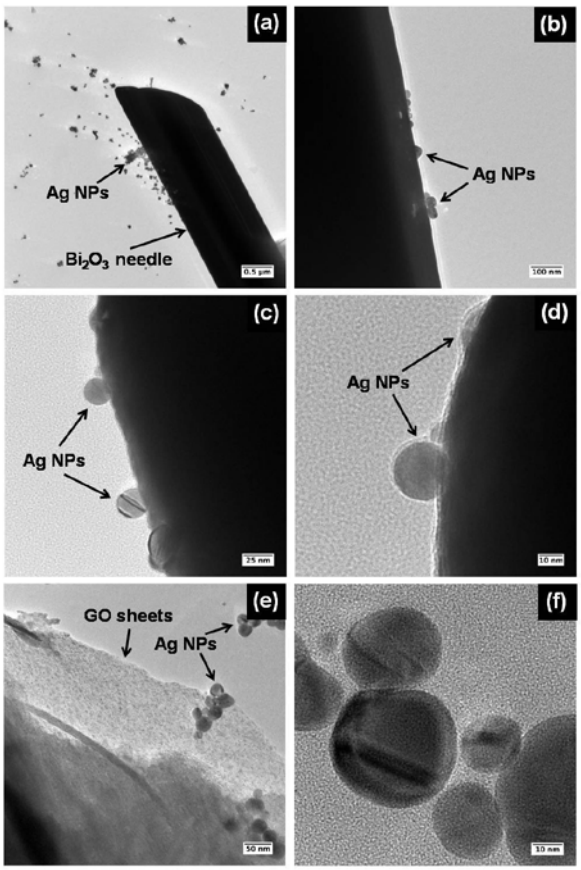


**The scale bars are much too small!**

**Figure 2.** TEM images of the sample Ag/GO/$Bi_2O_3$ showing (a) α-$Bi_2O_3$ needles and Ag NPs, (b-d) Ag NPs located on the surface of the α-$Bi_2O_3$ needle, (e) Ag NPs located on the surface of the GO sheets and (f) near-spherical Ag NPs at a higher magnification.

### Crystal Structure

The powder X-ray diffractions (XRDs) of the samples provide information about their crystal structure and are shown in **Figure**

**3**. The XRD pattern of GO (**Figure 3a**) shows a broad prominent peak at about 2θ = 10.34°. It corresponds to the (002) reflection of stacked GO sheets with a calculated interlayer (d-) spacing of 0.85 nm. It falls within the range of 0.75-0.94 nm reported for GO materials. [10] This calculated layer-to-layer distance is much larger than that obtained for the precursor graphite (0.34 nm). This further advocates the accommodation of various functional groups and $H_2O$ molecules between graphite lamellar structures after oxidation. [35]

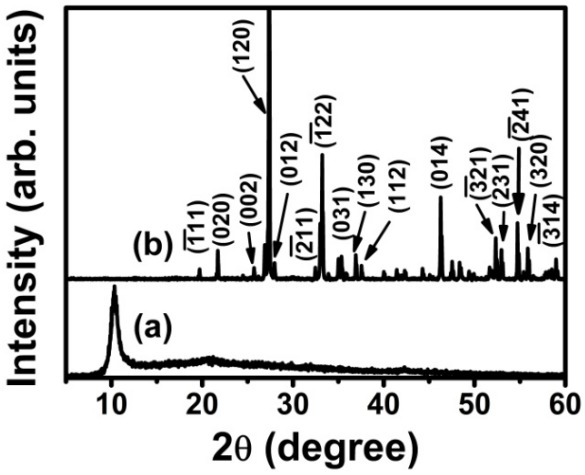


**Figure 3.** X-ray diffraction patterns of GO and GO/$Bi_2O_3$.

For the GO/$Bi_2O_3$ sample (**Figure 3b**), all the XRD peaks correspond to that of monoclinic α-$Bi_2O_3$ (JCPDS: 41-1149). Absence or disappearance of any GO or RGO peaks is due to their low content. It is also an indication that during the hydrothermal reaction, crystal growth of $Bi_2O_3$ between the inter-layers of GO leads to their easy exfoliation of GO and destroyed their regular stacking. Consequently, the Bragg diffractions peaks of GO cannot be recorded. The XRD pattern also illustrates that the presence of the GO sheets does not result in the development of new crystal phases of $Bi_2O_3$ or changes the preferential orientations of the α-$Bi_2O_3$ needles.

The XRD pattern of the Ag/GO/$Bi_2O_3$ sample is similar to that of GO/$Bi_2O_3$ in **Figure 3b**, except from the presence of small quantities of $Bi_2O_2CO_3$ (for details see supplementary information, **Figure S3**). This is probably because $Bi(NO_3)_3$ in nitric acid solution undergoes hydrolysis to produce soluble $BiONO_3$. The dissolved $CO_2$ present in water also undergoes hydrolysis to $CO_3^{2-}$ ions which further react with the $BiONO_3$ to form $Bi_2O_2CO_3$ according to **equation (1)**.[63]

$$2BiONO_3 + CO_3^{2-} \rightarrow 2NO_3^- + Bi_2O_2CO_3 \quad (1)$$

$Bi_2O_2CO_3$ is also a well-know semiconductor photocatalyst with the energy level of valence band ($E_{VB}$) and energy level of conduction band ($E_{CB}$) lying at 3.31 eV and 0.41 eV (vs. NHE), respectively. Although present in minor quantities, as evidenced in the XRD pattern (**Figure S3**), its role in the present photocatalytic system can envisaged similar to that of $Bi_2O_3$ due to its similar energy levels. No diffraction peaks of Ag are observed due to its extremely low content.

**Raman Spectra**

Raman spectroscopy provides a powerful probe to gain information about doping, number of layers, defects, and other structural and electronic insight in these kinds of materials. In **Figure 4**, the Raman spectra of GO and the different materials incorporating GO are shown.

The Raman spectrum of GO (**Figure 4a**) exhibits two prominent phonon modes. The D phonon mode located at v = 1330 $cm^{-1}$ and the G phonon mode located at v = 1586 $cm^{-1}$. The former arises from a breathing mode of κ-point phonons of $A_{1g}$ symmetry. It is related to disorder in the $sp^2$–hybridized carbon atoms, functional groups at the edges, lattice distortions, and other defects.[64-66] The latter indicates the presence of isolated double bonds and arises from first-order scattering of the tangential stretching ($E_{2g}$) phonon mode of $sp^2$- hybridized carbon atoms.[64-66]

The Raman spectra of the GO/$Bi_2O_3$ (**Figure 4b**) and Ag/GO/$Bi_2O_3$ (**Figure 4c**) composites show additional phonon modes in the low energy region. For both cases, they can be assigned to α-$Bi_2O_3$ (for details see supplementary information, **Figure S4**). [67] For the GO/$Bi_2O_3$ composite, GOs D and G phonon modes are located at v = 1338 $cm^{-1}$ and v = 1596 $cm^{-1}$ respectively. After the incorporation of Ag, in the Ag/GO/$Bi_2O_3$ composite, the GOs G phonon mode it is located at v = 1591 $cm^{-1}$ (**Figure 4, inset** provides the zoom of the G phonon mode frequency region).

In GO, p-type and n-type doping causes opposite shifts of the G phonon mode. Electron acceptor or donor molecules for example, give rise to mid-gap molecular levels with the possibility of tuning the band gap region near the Dirac point.[65] These molecules adsorbed onto the GO surface exhibit an effective charge transfer which is reflected in the described frequency shift of the G phonon mode. Electron-withdrawing organic groups (i.e. nitrobenzene) or p-type dopants offer hole-doping, cause the stiffening of the G phonon mode in GO and shift towards higher frequency.[68] Electron-donating groups in molecules adsorbed to GO (i.e. aniline) or n-type dopants offer electron-doping, cause softening of the G phonon mode and shift towards higher frequency. [69]

In the GO/$Bi_2O_3$ composite, the shift of the G phonon mode from v = 1586 $cm^{-1}$ to v = 1596 $cm^{-1}$ provides a convincing evidence of charge transfer from GO to p-type $Bi_2O_3$. Additionally, this blue-shift provides a clear evidence for anchoring (chemical bonding and hybridization) between $Bi_2O_3$ and GO sheets. [65,66] In case of the Ag/GO/$Bi_2O_3$ composite, the G phonon mode experiences a red-shift to v = 1591 $cm^{-1}$ and thus, lower frequency relative to the GO/$Bi_2O_3$ composite. This is because Ag acts as an electron donor component to GO. This provides a direct evidence of n-type doping by Ag. [69, 70] Thus it is reasonable to say that the resultant G phonon mode frequency in case of the Ag/GO/$Bi_2O_3$ composite, indicates the formation of heterostructured n/GO/p junction composites. This is further supported by the work functions of Ag (4.2 eV), [71] GO (4.70 eV),[11] and $Bi_2O_3$ (6.23 eV).[72] Since the work function of Ag is smaller than that of GO, electron transfer from Ag to GO sheets occurs by the creation of the Ag/GO/$Bi_2O_3$

heterostructures. This is followed by the electron transfer from GO to the conduction band of $Bi_2O_3$.

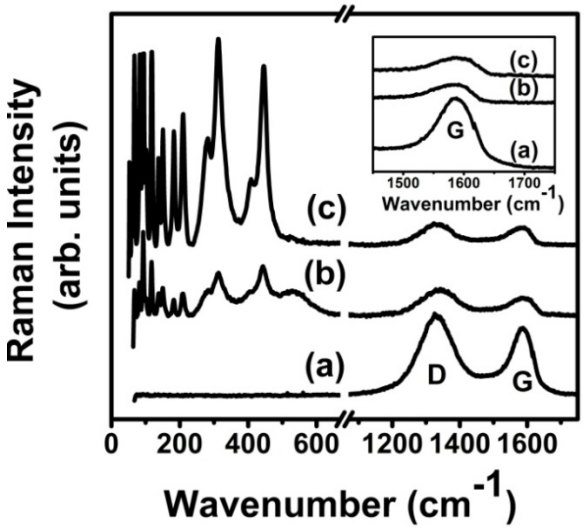


**Figure 4.** Raman backscattering spectra of (a) GO, (b) $GO/Bi_2O_3$ composite and (c) $Ag/GO/Bi_2O_3$ composite. The inset shows by way of comparison the positions of graphene oxide G phonon modes.

The $I_D/I_G$ ratio is proportional to the average size of $sp^2$ domains and thus is a measure of the degree of disorder in graphene based materials. The $I_D/I_G$ intensity ratio of GO is 1.20. However, this value increases to 1.25 for the GO/α-$Bi_2O_3$ composite and is 1.50 in the case of the Ag/GO/α-$Bi_2O_3$ composite. This indicates a decrease in the average size of the $sp^2$-domains upon composite formation. The higher $I_D/I_G$ ratio for the Ag/GO/α-$Bi_2O_3$ composite indicates further introduction of defects and disorder in the GO sheets. This appears as a result of deposition or trapping of some Ag NPs on vacancies of the GO sheets due to the interaction with the dangling bonds.

**Photocatalytic Performance**

The photocatalytic activities of the synthesized composites are determined by evaluating their percent degradation in decolorizing and mineralizing the model non-biodegradable organic pollutants, crystal violet (CV) and rhodamine 6G (Rh6G), under visible light irradiation (300 W tungsten incandescent lamp) and the results of time-dependent percent degradation are shown in **Figure 5(a-b)**.

Commercial $TiO_2$ (Degussa P25) is chosen as the reference photocatalyst for performance comparison. The change in intensity of the main absorbance peak ($A_0$) with time ($A_t$) at 590 nm for CV and 525 nm for Rh6G were monitored under visible-light irradiation. A typical sequence of gradual disappearance of the characteristic absorption band of CV and Rh6G due to the photocatalytic degradation is provided in the supplementary as **Figure S5**.

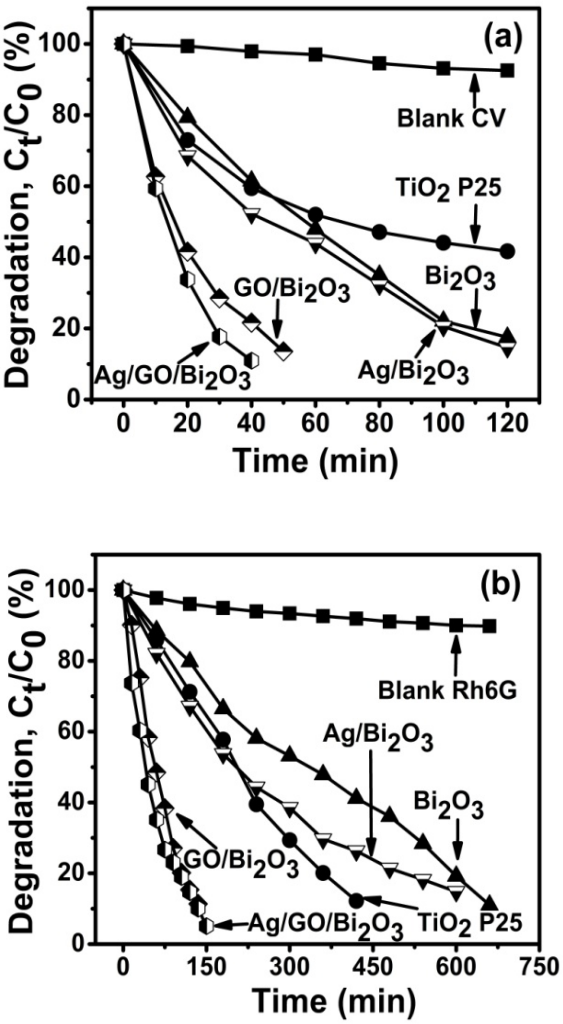


**Figure 5.** Comparison of photocatalytic activity of the different samples for the degradation of (a) CV, and (b) Rh6G as a function of visible light irradiation, where $C_0$ and $C_t$ are the initial and actual concentration of the dyes at different reaction times (t), respectively.

Most photocatalytic reactions follow the Langmuir-Hinshelwood adsorption model [73] which can be simplified into a pseudo-first-order expression: $\ln(C_0/C_t) = kt$ (where $C_0$ and $C_t$ are the initial equilibrium concentration of the adsorbed dye and the concentration of the dye after illumination time, t, respectively and is proportional to the normalized absorbance $A_0$ and $A_t$, and k is the apparent rate constant). Using regression-fitting techniques the linear plots of $\ln(C_0/C_t)$ versus irradiation time t are attained. **Table 1** summarizes the calculated rate (k), the corresponding correlation coefficient (R) and reaction rate ratio. The photocatalytic reaction rate of GO/α-$Bi_2O_3$ composite

is 4-6 times greater than $TiO_2$ P25 in the degradation of Rh6G and CV, respectively. With the incorporation of Ag, it can be increased up to 8 folds over $TiO_2$ P25. The possible mechanism of photocatalytic degradation of organic dyes considering the energy level diagrams of GO, α-$Bi_2O_3$ and Ag NPs is elucidated in **Figure 6**.

**Table 1.** Degradation Rate Constants of Crystal Violet (CV) and Rhodamine 6G (Rh6G) dyes with Different Catalysts.

| Photocatalyst | Linear Equation | Rate, k [$min^{-1}$] | R | Ratio |
|---|---|---|---|---|
| **For CV dye** | | | | |
| $TiO_2$ P25 | $\ln(C_0/C_t)$=.00690t+ 0.14823 | 0.00690 | 0.987 | 1 |
| α-$Bi_2O_3$ | $\ln(C_0/C_t)$=0.01488t-0.07138 | 0.01488 | 0.998 | 2.16 |
| Ag/α-$Bi_2O_3$ | $\ln(C_0/C_t)$=0.01550t-0.00197 | 0.0155 | 0.994 | 2.25 |
| GO/α-$Bi_2O_3$ | $\ln(C_0/C_t)$=0.03876t+ 0.05252 | 0.03876 | 0.998 | 5.62 |
| | | | | |
| **For Rh6G dye** | | | | |
| $TiO_2$ P25 | $\ln(C_0/C_t)$=0.00413t– 0.08690 | 0.00413 | 0.986 | 1 |
| α-$Bi_2O_3$ | $\ln(C_0/C_t)$=0.00211t+0.00363 | 0.00211 | 0.998 | 0.51 |
| Ag/α-$Bi_2O_3$ | $\ln(C_0/C_t)$=0.00316t+0.02476 | 0.00316 | 0.999 | 0.76 |
| GO/α-$Bi_2O_3$ | $\ln(C_0/C_t)$=0.01542t+0.11998 | 0.01542 | 0.990 | 3.73 |
| Ag/GO/α-$Bi_2O_3$ | $\ln(C_0/C_t)$=0.01578t+0.05591 | 0.01578 | 0.997 | 3.82 |

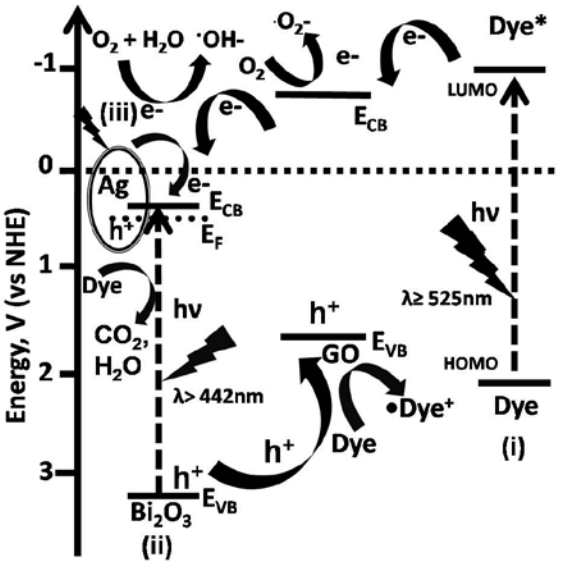


**Figure 6.** Energy-level diagram in relation to the redox potentials and schematic illustration of the photocatalytic organic dye degradation for Ag/GO/$Bi_2O_3$ composite showing the three different possible simultaneous light-induced excitation pathways (i) dye-excitation, (ii) $Bi_2O_3$ excitation and (iii) Ag plasmon excitation. This is subsequently followed by (a) electron-hole formation and transfer, (b) reactive species formation and (c) dye degradation.

Upon illumination, two possible electronic pathways may follow: (i) the semiconductor is excited and the electron is promoted to the CB creating a hole in the VB [$Bi_2O_3$ + hu → $Bi_2O_3$* ($h^+_{VB}$ + $e^-_{CB}$)] and (ii) the dye is excited [dye + +hu → dye*].

The enhanced photocatalytic activity of $Bi_2O_3$ can be attributed to the favorably located energy levels of $Bi_2O_3$ that result in easy formation of highly reactive hydroxyl radicals ($^{\bullet}OH^-$) that participate in the photo driven reactions. The $O_2$ reduction potential for the single-electron reduction process: $O_2$ + $e^-$ → $^{\bullet}O_2^-$ is -0.28 V vs. NHE whereas for the multi-electron reduction process: $O_2$ + $2H_2O$ + $4e^-$ →$4^{\bullet}OH^-$ is +0.40 V vs. NHE).[66] For $Bi_2O_3$, the energy level $E_{CB}$ lies at +0.33 V vs. NHE. This is exactly in the potential range for the multi-electron reduction of $O_2$. Thus the electrons in the $E_{CB}$ of $Bi_2O_3$ can effectively be transferred to the adsorbed $O_2$ to form $^{\bullet}OH^-$ radical. On the contrary, the band gap ($E_g$) of $TiO_2$ is 3.0-3.2 eV and its $E_{CB}$ lies at -0.3 V vs. NHE. So, for $TiO_2$, the $O_2$ is likely to be reduced by single-electron process. Moreover, the holes in the valence band ($h^+_{VB}$) of $Bi_2O_3$ have enough positive potential to generate hydroxyl radicals: $h^+_{VB}$ + $H_2O$ → $H^+$ + $^{\bullet}OH^-$.

The higher efficiency of α-$Bi_2O_3$ may also be due to the distorted Bi-O polyhedron structure induced by the $6s^2$ lone pair of $Bi^{3+}$. Asymmetric coordination environment facilitates effective surface migration of carriers and retard exciton recombination.[74-76] Monoclinic $BiVO_4$ with Eg 2.41 eV is also found to display higher photocatalytic activities than tetrahedral $BiVO_4$ with Eg 2.34 eV.[76]

Apart from the band-gap, another very important factor which governs the photocatalytic activity of the semiconductor is the availability of number of surface active sites and oxygen vacancies. $TiO_2$-P25 shows lower activity in comparison with $Bi_2O_3$ for degradation of CV. This is probably owing to the loss of surface active sites of $TiO_2$-P25 due to surface poisoning effects

after prolonged treatment (adsorption) with CV. On the contrary, we consider Rh6G to result in loss of surface active sites of $Bi_2O_3$, which reduces its overall efficiency relative to $TiO_2$ in Rh6G degradation.

In absence of GO, the photosensitized dye* can inject photoexcited electrons directly in the $E_{CB}$ of $Bi_2O_3$ thereby leading in reactive radical formation and resulting in a self-degradation pathway under visible light irradiation. The holes can also combine with the dye to form unstable radical species: $h^+_{VB}$ + dye → $^{\bullet}dye^+$. Thus, the dye undergoes oxidation followed by degradation.

With the introduction of Ag, the photocatalytic activity of the composite is improved as compared to bare $Bi_2O_3$ needles. Although Ag is widely recognized as an electron scavenger, however in case of Ag/$Bi_2O_3$ composite, Ag cannot be a co-catalyst with the normal electron-scavenging function. We show that in the present case, the Ag NPs act as visible-light harvesting nano-antennas. They are small enough to exhibit plasmon-photoexcitation and act as electron-generating centres. Metal particles such as Ag and Au have a Fermi level ($E_F$) at 0.4 V versus NHE. [77] The band structure of the $Bi_2O_3$ supports the transfer of photogenerated plasmonic electrons from Ag to the $E_{CB}$ of $Bi_2O_3$ (0.33 eV). Thus, the Ag/$Bi_2O_3$ composites support the model of plasmonic photocatalyst. This is similar to the Pt/$Bi_2O_3$ system reported by Li et al.[78] The photons absorbed by the Ag NPs are economically separated into electrons and holes. While the electrons are transferred to the $E_{CB}$ of $Bi_2O_3$, the holes diffuse on the surface of the Ag NPs where they take part in the decomposition of organic matter. Moreover, the deposition of minute crystalline Ag NPs on the surface of these $Bi_2O_3$ needles is expected to bring about small changes on the surface microstructure of Ag/$Bi_2O_3$ composite, improve the crystallinity, increase the number of available active sites, and thereby enhance the dye adsorption.

The remarkable enhancement of the photocatalytic activity with introduction of GO sheets is due to the synergistic effects between $Bi_2O_3$ and the GO. It has been reported that the $E_{CB}$ of GO does not change with the degree of oxidation. Thus GO samples with different oxidation levels have a $E_{CB}$ at about -0.75 V (vs. NHE). [4,79,80] From the indirect transition energy plot of our GO samples, the band gap was determined to be in the range of 1.48–2.28 eV (refer to **Figure S6** and Band Gap Determination of GO in the supplementary) So the $E_{VB}$ maximum is at 1.48 V (vs. NHE). The band structure of GO is constructed (**Figure 6**) based on the above $E_{CB}$ and $E_{VB}$ levels.

The GO sheets function as adsorption mats providing higher surface area and result in enhanced dye adsorption. The strong affinity of GO to the aromatic dye molecules is due to π–π interactions as well as ionic and dipolar interaction. Besides, the GO can be considered to possess some ionized carboxylic acid groups also. So, cationic dye molecules can also be adsorbed via electrostatic force field interaction.[25,81]

The GO sheets act as electron scavengers accepting photoexcited electrons from the excited dye, which they can delocalize over their π-orbitals. There are several convincing evidences in literature in support of the electron transfer from photochemically generated dye radicals to GO. [82,84] Thus, high electron density develops over the GO sheets. The electrons are then transferred to the $E_{CB}$ of $Bi_2O_3$. This transfer process, when GO and $Bi_2O_3$ are in contact, is supported by the Raman spectra (**Figure 4**) and the literature work function values. A recent density functional calculation study has shown that charge transfer from excited graphene to the $E_{CB}$ of rutile titania is possible and results in the hole doping in graphene.[84] This behaviour may be viewed similar to that of $TiO_2$/CNT hybrids where electrons from sensitizer CNT are injected into $E_{CB}$ of $TiO_2$.[85]

In case of Ag/GO/$Bi_2O_3$, the GO also act as an electron-shuttle transferring plasmonically excited electrons from Ag to $Bi_2O_3$. This information can be directly derived from our Raman spectra (**Figure 4**). In a very recent report on the photocatalytic activity of CNT/Ag/AgBr composite, CNTs were shown to exhibit a similar electron-shuttling and transferring function and promote electron–hole pairs separation.[86]

The resultant high concentration of electrons finally available in the $E_{CB}$ of $Bi_2O_3$ favours the multi-electron reduction process. Some electrons available in the $E_{CB}$ of GO may also participate in the single electron reduction process of $O_2$. The holes generated in the $E_{VB}$ of $Bi_2O_3$ upon visible light excitation are readily transferred to the $E_{VB}$ of GO. Consequently, the lifetimes of the holes are increased and they participate in the dye mineralization process. Moreover, the high concentrations of adsorbed dye molecules, preferentially over the GO surface, can speed up the reaction with the aid from photogenerated reactive species.

**Structural Modification after Photocatalysis**

The GO sheets act like fishing-nets absorbing large quantities of the dye from the solution. Therefore, in order to confirm that the reduction of the pollutant concentration is essentially due to photocatalytic degradation, the Fourier-Transform Infrared (FT-IR) spectra of the photocatalyst Ag/GO/$Bi_2O_3$ are determined before and after the photocatalytic reactions.

Firstly, in Figure 7 (curve a), the FT-IR spectrum of GO sheets is recorded which confirm the presence of different oxygen containing functionalities which are responsible for anchoring different particles of $Bi_2O_3$ and Ag over them. For GO, the intense absorption band at 3391 $cm^{-1}$ is due to hydroxyl O-H stretching vibration. The band at 1732 $cm^{-1}$ indicates the C=O stretching vibration of the COOH groups. The 1618 $cm^{-1}$ band arises due to skeletal vibrations from unoxidized graphitic domains. The 1406 $cm^{-1}$ band originates due to the tertiary C–OH stretching vibration and 1030 $cm^{-1}$ indicates the C–O stretching vibration. [87] In Figure 7 (curve b), the set of bands below 600 $cm^{-1}$ arises due to Bi-O vibrations in $Bi_2O_3$. [88,89]

The FT-IR spectra of the sample Ag/GO/$Bi_2O_3$ before (curves c) and after (curves d and e) the photocatalytic reactions are being compared. The FT-IR spectrum of Ag/GO/$Bi_2O_3$ hybrid composite (Figure 7, curves c) represents bands arising due to both Bi-O vibrations of $Bi_2O_3$ and bands due to vibrations of the different functional groups of GO. The small band at 846 $cm^{-1}$ in the in case of the Ag/GO/$Bi_2O_3$ composite may be due to the presence of small amount of $Bi_2O_2CO_3$ formed during the synthesis of the material as mentioned before (refer equation 1). This $v_2$ mode $CO_3^{2-}$ band at 846 $cm^{-1}$ is intensified for the Ag/GO/$Bi_2O_3$ composite collected after the photocatalytic reactions (Figure 7, curves d and e). In addition there is

appearance of strong bands at 1380 and 1472 $cm^{-1}$. These two peaks can be assigned to the $v_3$ vibrational mode of the $CO_3^{2-}$ group. [40,88,90]

$CO_2$ is generated as one of the end products of the mineralization process of the organic compounds.[15] In presence of $^{\bullet}OH^{-}$ radical, which is also generated during the photocatalytic process, the $CO_2$ forms bicarbonate species in solution which further reacts with the $Bi_2O_3$ during the period of prolonged irradiation to form $(BiO)_4CO_3(OH)_2$ and finally $Bi_2O_2CO_3$. These are possibly deposited on the surface sites of the $Bi_2O_3$. The transformation from $Bi_2O_3$ to $Bi_2O_2CO_3$ in water containing $CO_2$/ $HCO_3^-$ has been observed by Huang et al. [88] Moreover, photoinduced structural transformations of oxide semiconductor into carbonates during photodegradation of methyl orange azo dye have been observed by Yang et al. [91] Marinho et al [92] observed the transformation of $Bi_2O_2CO_3$ back to $Bi_2O_3$ upon calcination. Thus, the time, irradiation and pH dependent structural modification of the photocatalyst along with the influence of intermediate reaction products during the photocatalytic reaction at regular intervals, being significant with regard to the performance of the $Bi_2O_3$-based photocatalysts, demand further intensive investigations.

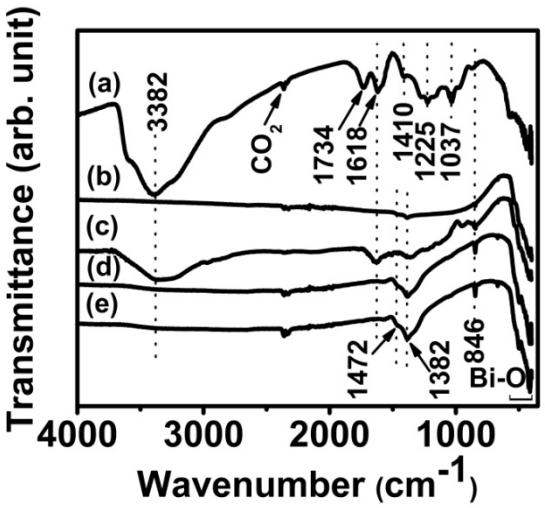


**Figure 7.** FT-IR spectra of (a) GO, (b) α-$Bi_2O_3$ needles, (c) Ag/GO/ α-$Bi_2O_3$, (d) dried Ag/GO/ α-$Bi_2O_3$ photocatalyst recovered after photodegradation of CV dye and (e) dried Ag/GO/ α-$Bi_2O_3$ photocatalyst recovered after photodegradation of Rh6G dye.

**Catalytic Performance**

Noble metal NPs possess excellent catalytic properties and are known to catalyze the reduction of 4-nitrophenol (4-NP) to 4-aminophenol (4-AmP) in presence of $NaBH_4$ at 0ºC.[93] As semiconductor NPs are generally inactive towards this reaction, therefore, the presence of Ag (metal) doping in Ag/$Bi_2O_3$ and Ag/GO/$Bi_2O_3$ composites are expected to be indicated by their positive catalytic response.

Under neutral or acidic conditions, 4-NP exhibits an absorption peak at 317 nm. The $NaBH_4$ addition results in formation of 4-nitrophenolate ions which results in red-shift of the absorption peak to about 400 nm. As the metal NPs catalyze the formation of 4-AmP, the intensity of the 4-nitrophenolate absorption peak at 400 nm gradually decreases while a new peak emerges at 298 nm corresponding to 4-AmP.[67,93]

However, in the present case, $NaBH_4$ reduces the $Bi_2O_3$ needles to metallic $Bi^0$ needles and the GO to RGO or graphene. In our previous study, we have demonstrated for the first time that Bi particles (micro-hexagons) display positive catalytic activity towards this reaction.[67] Consequently, the catalytic activities are recorded for all samples. This is due to the in-situ chemical reduction of α-$Bi_2O_3$, Ag/$Bi_2O_3$, GO/$Bi_2O_3$ and Ag/GO/$Bi_2O_3$ into $Bi^0$, $Ag^0/Bi^0$, RGO/$Bi^0$ and $Ag^0$/RGO/$Bi^0$ composites by $NaBH_4$. A representative time dependent absorption spectra showing the conversion of 4-NP into 4-AmP is shown in **Figure S7**.

The rates of catalytic activities are evaluated for these pseudo-first-order reactions by plotting $\ln(A_t/A_0)$ versus time (t), where $A_t$ and $A_0$ are the absorbances at 400 nm at times t and 0 (**Figure 8**). The rate or activity is found to increase in the order: $Bi^0$ < $Ag^0/Bi^0$ < RGO/$Bi^0$ < $Ag^0$/RGO/$Bi^0$ (in ratio: 1< 2.5 < 7 < 9.7 folds) (refer to inset of **Figure 8**). It must be mentioned here that Bi and Ag forms a low melting eutectic mixture with 2.5% Ag.[93] Therefore, the formation of Ag-Bi some alloy even with very low concentration of Ag atoms (2 %) with surface segregation of Ag atoms under the present experimental conditions cannot be overruled. Interestingly, even after reduction, the specific morphologies of the composites are retained, as seen from the SEM image in **Figure S8**.

The high activities of the RGO doped composites is due to the fact that the intercalated graphene sheets act as adsorption mats for the 4-NP via π-π stacking interactions. This enables a high concentration of 4-NP around Bi and Ag particles for effective reduction. In absence of graphene mats, the reaction rate is slower as it depends on the probability of collision of the 4-NP molecules with the metal particles. 4-NP molecules which do not collide with the metal particles can pass back into solution.[95,96]

This reaction gives an indication that although noble metal particles (Ag) are catalytically more active than heavy metal particles (Bi) but the introduction of graphene has a dramatic effect. Composite materials of Bi nanometal and its intermetallic alloys (Bi-Ag) incorporated on RGO sheets have superior activity and deserve further investigation due to its potential as replacing the noble metal catalysts.

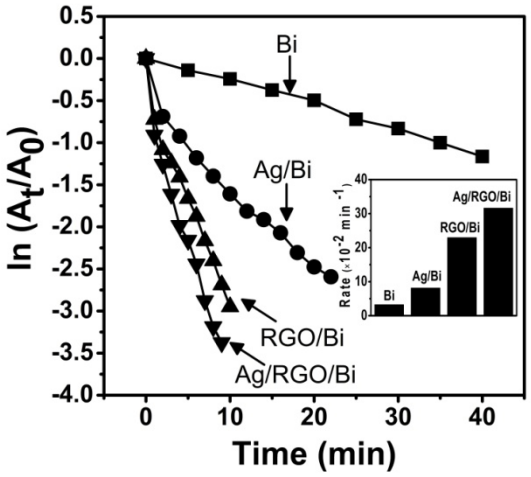


**Figure 8.** Plot of $\ln(A_t/A_0)$ versus and evaluation of rate constants for the catalytic reduction of 4-nitrophenol by $NaBH_4$ in presence of different composites, where $A_0$ is the initial normalized absorbance and $A_t$ is absorbance after time (t). The inset shows a comparative bar graph elucidating the different rates for different samples.

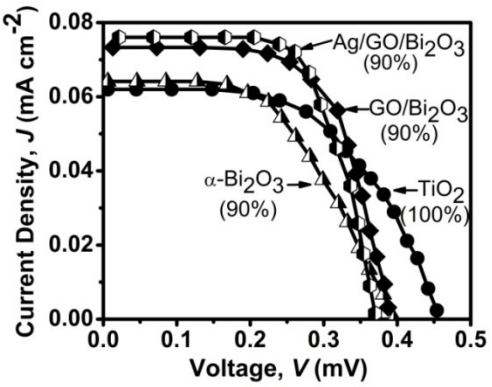


**Figure 9.** The photocurrent density-voltage (J-V) curves for different photoanodes. In all three cases of $Bi_2O_3$, $GO/Bi_2O_3$ and $Ag/GO/Bi_2O_3$, the remaining 10% (by weight) was commercial $TiO_2$ paste acting as an auxiliary binding agent (see photoanode preparation in the experimental section).

**Performance as Photoanodes**

Dye-sensitized solar cells (DSSC) have emerged as the most economical assembly for indoor photovoltaic applications and educational purposes. To study the performance of these composite materials as photoanodes in DSSCs, we use $TiO_2$ as a secondary binding agent (for details refer to the Experimental Section). The advantages of $TiO_2$ which make it suitable for DSSC applications are (i) the position of its CB with respect to the redox potential of the well-known $I_3^-/I^-$ system (0.4 V vs NHE) which enables extraction of high open-circuit photovoltage ($V_{OC}$) values. [97] The Voc is related to the energy difference between the quasi-Fermi level of electrons in the semiconductor and the chemical potential of the redox mediator in the electrolyte (schematically depicted later in **Figure 10**). Higher $V_{OC}$ can help to extract higher fill-factor (FF) value and thereby higher photoconversion efficiency (η). (ii) $TiO_2$ has higher isoelectric point (IEP) than $Bi_2O_3$. The pHiep $TiO_2$ ≈ 5.2 [98] while $pH_{iep}$ $Bi_2O_3$ ≈ 3.2). [99] The IEP is the pH value at which the metal oxide surface carries no net electric charge and is an important surface property that determines the dye metal-oxide interface in the DSSC. The metal oxide surfaces bear a net positive charge at a pH below the IEP and a net negative charge above the IEP. Particles with higher $pH_{iep}$ values show higher dye loading abilities.[100] $Bi_2O_3$ needs longer time for dye loading.

In **Figure 9**, the photoinduced photocurrent density-voltage (J-V) curves are presented. These are used to evaluate the energy conversion properties of the DSSCs. The photovoltaic properties of the different photoanodes are tabulated in **Table 2**.

The DSSC with $Bi_2O_3$ containing electrode shows a short-circuit photocurrent density (Jsc) of 0.064 $mAcm^{-2}$ and an overall energy conversion efficiency (η) of 0.013 %. The introduction of GO leads to an enhancement of both $J_{SC}$ and η by 14% and 20% respectively, with respect to the $TiO_2$ photoanode, as evident form **Table 2**. The presence of 2wt% Ag NPs in the $Ag/GO/Bi_2O_3$ electrodes further increases $J_{SC}$ and η by ~ 4 and ~ 6 % in comparison with the $GO/Bi_2O_3$ anode. The main reason for the rise in η value is due to the increase in the FF and $J_{SC}$. It is therefore interesting to note that both anodes, $GO/Bi_2O_3$ and $Ag/GO/Bi_2O_3$, display better performances than the commercial $TiO_2$ anode.

**Table 2.** Photovoltaic properties of four different photoanodes.[a]

| Photoanodes[b] | $J_{SC}$ [mA $cm^{-2}$] | $V_{OC}$ [mV] | FF | η % |
|---|---|---|---|---|
| Commercial $TiO_2$ paste (reference) | 0.062 | 0.454 | 0.549 | 0.015 |
| α-$Bi_2O_3$ : $TiO_2$ = 9:1 | 0.064 | 0.396 | 0.523 | 0.013 |
| GO/α-$Bi_2O_3$ : $TiO_2$ = 9:1 | 0.073 | 0.388 | 0.646 | 0.018 |
| Ag/GO/α-$Bi_2O_3$ : $TiO_2$ = 9:1 | 0.076 | 0.370 | 0.672 | 0.019 |

[a] $J_{SC}$ = short-circuit current, $V_{OC}$ = open-circuit photovoltage, FF = fill factor , η = photoconversion efficiency. [b] See experimental details and calculation of FF and η values

In **Figure 10**, the fundamental working mechanism of our DSSCs is presented. It is expected that in the anode, the electrons are injected from the LUMO of the sensitized anthocyanin dye into the $E_{CB}$ of $TiO_2$, followed by electrons

injection into the $E_{CB}$ of $Bi_2O_3$. The electrons are transported through the semiconductor layers by diffusion to reach the conducting ITO glass substrate and thereby to the outer circuit. This electron flow is assisted by the partially reduced GO sheets. At the carbon coated counter electrode, the oxidized species of the redox electrolyte, i.e. $I_3^-$ ions in iodide-triiodide complex, is reduced to $I^-$. The $I^-$ ion now donates an electron to the oxidized dye ($D^+$) and regenerates the dye molecule. The above processes go in cycle resulting is a continuous current flow through the external circuit as long as light is incident on the cell.

The possibility of improvement of $J_{SC}$ and performance by incorporation of graphene-based structures is quite noticeable. Firstly, GO causes in increased absorption of dye molecules. More dye molecules are expected to harvest more light energy. Secondly, the GO provides efficient electron transfer pathways to the ITO surface. Thus the electrons are rapidly collected before being recombined. The resistance of GO sheets are usually about ~1 × $10^5$ Ω $\square^{-1}$. [101] $TiO_2$ films may exhibit resistances of about ~$10^7$ Ω $\square^{-1}$.[102] $Bi_2O_3$ films have resistance ~ $10^6$ Ω $\square^{-1}$.[103]

It must be mentioned here that there is considerable scope for the improvement of $J_{SC}$ in DSSC by designing thin layers and structures which reduces the electron diffusion length and improves carrier mobilities, which depend on the film morphologies.[104] The carefully designed thin layers would result in less charge depletion and back electron transfer (recombination processes R1, R2, R3 and R4 as shown in **Figure 10** with dotted lines). Finally, the use of competent dyes[105] improving the interfacial contact between $TiO_2$ and $Bi_2O_3$, their crystallinity, and decreasing the resistivity of GO by their selective conversion into graphene [106,107] intercalated sheets is expected to improve their behavior.

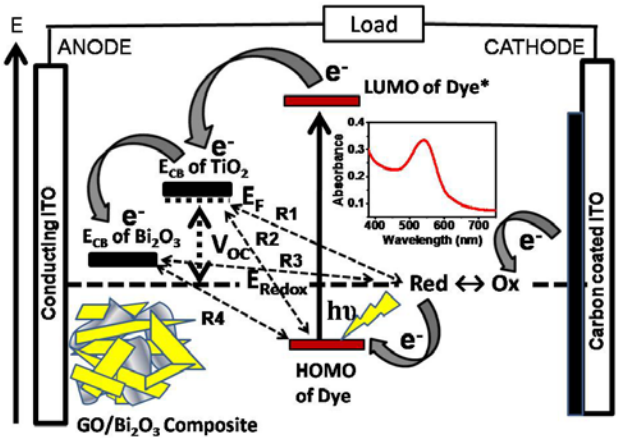


**Figure 10.** Schematic representation of the fundamental working principle of our dye sensitized solar cell. The inset shows the absorption spectrum of the anthocyanin dye. After excitation of the dye (HOMO → LUMO), the electrons can be transferred sequentially to the $E_{CB}$ of $TiO_2$, to $E_{CB}$ of $Bi_2O_3$, to the anode. This process is assisted by the partially reduced GO sheets. The transfer continues to the cathode and finally to the redox couple, thus completing the cycle with an idealized 100 % quantum yield. R1, R2, R3 and R4 are the competing electron recombination processes which dramatically reduce the obtainable efficiency.

## Conclusions

To summarize, we have presented a facile single-step green chemical synthesis strategy to prepare multifunctional GO/α-$Bi_2O_3$ and Ag/GO/α-$Bi_2O_3$ hybrid composites. Our strategy circumvents the use of any toxic precursor reagents. We have fully characterized these heterostructured composites by SEM, XRD and Raman spectroscopy and exploited their applications towards photocatalysis, harvesting solar energy and catalysis.

The photocatalytic activities of $Bi_2O_3$ in the degradation of organic pollutants (crystal violet and rhodamine 6G) enhance by ~4-6 folds when hybridized with only 1.0 wt% graphene-based structures as compared to the commercial $TiO_2$-P25. With the incorporation of Ag doping (2.0 wt% Ag), the photocatalytic efficiency further increases over 8 folds. We discuss the photocatalytic degradation mechanism in view of plasmonic photocatalysis. We propose that the photogenerated electron–hole pairs are formed on the surface of the minute Ag particles owing to plasmonic excitation effect under visible irradiation. These electrons are instantly transferred to the favourably located energy levels of the conduction band in $Bi_2O_3$. The small amount of GO sheets is highly beneficial for the photo-generated electron transfer from Ag to $Bi_2O_3$, as evidenced by the Raman data. The GO sheets also allow strong adsorption of aromatic dye molecules and therefore immensely enhance the photocatalytic activity.

We further extend the applications of these hybrid composites in (i) catalysis and (ii) dye sensitized solar cells (DSSC). GO/$Bi_2O_3$ composites can be reduced to RGO/$Bi^0$ composites by $NaBH_4$. The RGO/$Bi^0$ shows ~7 times increased catalytic performance in 4-aminophenol to 4-nitrophenol conversion reaction than metallic $Bi^0$ with similar needle morphology. This enhancement is possibly due to a synergistic effect. The catalytic performances of $Ag^0/Bi^0$ and $Ag^0$/RGO/$Bi^0$ composites have also been compared and it turns out that a very small amount of noble metal (2 wt% of Ag) in $Ag^0$/RGO/$Bi^0$ composite is the most efficient one. Both the short circuit photocurrent density and overall energy conversion of DSSC with GO/$Bi_2O_3$ and Ag/GO/$Bi_2O_3$ electrodes increase by ~ 20 % as compared with commercial $TiO_2$ electrodes. The electronic interaction between GO and $Bi_2O_3$ is mainly considered to be responsible for the enhanced photocurrent conversion.

For future research, we essentially emphasize here the advantages of using $Bi_2O_3$-based ecofriendly materials as an efficient contender of commercial $TiO_2$-P25 with regard to visible light photocatalysis. The possibility of using $Bi_2O_3$ as plasmonic photocatalyst, when combined with metal NPs like Ag, is also highlighted. The band positions of $Bi_2O_3$ favor the fabrication of plasmonic photocatalysts. At the same time, we demonstrate the possibility of using $Bi_2O_3$ as an electrode material in dye sensitized solar cells when combined with $TiO_2$. The photocurrent generation and power conversion efficiency enhances by 14 and 20% respectively upon incorporation of GO. Finally, we draw the attention of our readers towards partial replacement of the noble metal catalysts. Catalysis with heavy metal (Bi)-graphene composites has been shown to possess significant potential in the emerging research-area of “reduced usage of noble-metals in catalysis”. Overall, both the graphene oxide and the graphene have been demonstrated to act as an efficient promoter in photocatalysts, photoanodes and catalysts.

## Experimental Section

**Synthesis of Graphene Oxide**. The precursor GO is synthesized by modified Hummers' method. 0.5 g of graphite was oxidized with 0.5 g of $NaNO_3$, 23 mL of 98% $H_2SO_4$ (JT Baker), and 3 g of $KMnO_4$ in an ice bath. 46 mL of slowly water was slowly added and the mixture was kept at 95 °C for 1 h under continuous stirring. The unreacted $KMnO_4$ was removed by the addition of 10 mL of $H_2O_2$. The oxidized graphite was purified by washing with 10% HCl (JT Baker) and a solvent-mix ($H_2O$/EtOH 1:5), and dried at 60 °C under vacuum. Exfoliation was accomplished by sonicating the GO aqueous solution for 120 min.

**Synthesis of Hybrid Composites.** The α- $Bi_2O_3$ needles and GO/α-$Bi_2O_3$ composite were prepared by hydrolysis of 0.5M $Bi(NO_3)_3{\cdot}5H_2O$ (Aldrich) solution in 1M $HNO_3$ (JT Baker) and in combination of the acidic solution of exfoliated GO (1 wt%) by 2M NaOH solution at 80°C.

$$2Bi(NO_3)_3.5H_2O + 6NaOH \rightarrow Bi_2O_3 + 6NaNO_3 + 8H_2O \quad (2)$$

The α-$Bi_2O_3$/Ag (yellowish-brown) and GO/ α-$Bi_2O_3$/Ag (greyish) composites are prepared by heating the un-doped composites in $AgNO_3$ solution (2 wt% Ag) at 80 °C under vigorous stirring for 2 h.

$$4AgNO_3 + 2H_2O \rightarrow 4Ag^0 + O_2 + 4HNO_3 \quad (3)$$

This forms the underlying principle of the $O_2$ evolution reaction by a semiconductor photocatalyst from an aqueous $AgNO_3$ solution.[108] The Ag-undoped nanocomposites were repeatedly washed prior use with diluted $HNO_3$ (1 %) solution followed by water to make them NaOH free. This is because the adhered NaOH may undergo double-decomposition reaction with the $AgNO_3$ to produce AgOH and thereby $Ag_2O$ upon warming, based on the following reaction

$$AgNO_3(aq) + NaOH(aq) \rightarrow AgOH(s) + NaNO_3(aq) \quad (4)$$

$$2AgOH \rightarrow Ag_2O + H_2O \quad (5)$$

$Ag_2O$ is an emerging well known photocatalyst. $Ag_2O$ is known to decompose to metallic Ag only at temperatures ≥ 330 ºC or under irradiation.

$$2Ag_2O \rightarrow 2Ag + O_2 \quad (6)$$

**Characterization.** The UV/Vis absorption spectra were recorded with a HR2000 UV/Vis spectrophotometer (Ocean Optics, Germany). SEM images were obtained using a TM-1000 tabletop-SEM (Hitachi, Japan). Samples for TEM observation were prepared by dropping the products on a carbon-coated copper grid after ultrasonic dispersion in ethanol/water mixture (1:1) and allowing~~ed~~ them to dry in air before analysis. TEM measurements were carried out ~~with TEM measurements were carried out with~~in a LIBRA 200FE (Carl Zeiss AG, Germany) operated at 200 kV using its in-column energy filter for zero loss filtered imaging (please ask Robert whether he used the filter, but in general he should have). XRD measurements were carried out using D8 Discover (Bruker AXS, Karlsruhe, Germany) with Cu $K_{\alpha 1}$ radiation (α = 1.5374 Å) with an operating current of 40 mA and a voltage of 40 kV, with a scanning rate of 5 s per step. Micro Raman measurements were obtained using a Princeton Instruments spectrometer (Roper Scientific, Germany) equipped with a low-power laser (5 mW) red 633 nm monochromatic excitation source. FT-IR spectra were recorded with VERTEX 70 spectrometer (Bruker, Germany) with an ATR diamond unit.

**Photocatalytic Activity Evaluation Set-up.** To determine the photocatalytic activity, 0.2 g of photocatalysts were added to 50 mL of aqueous solution of the dyes (a) crystal violet (CV, Aldrich) and (b) rhodamine 6G (Rh6G, Aldrich), each having concentration of $1 \times 10^{-5}$ $molL^{-1}$ contained in a closed borosilicate container. Prior to the irradiation, the suspensions were magnetically stirred in the dark for 30 min to ensure adsorption/desorption equilibrium. Thereafter, the borosilicate glass photoreactors are exposed to a 300 W tungsten incandescent lamp as the illumination source. The spectral range of tungsten filament lamp is 350-2500 nm and mainly consists of a large part of visible radiation. The dye solutions were also maintained at ice-cold conditions to prevent evaporation or any thermal decomposition. Commercial titanium dioxide $TiO_2$-P25 (20% rutile and 80% anatase) nanopowder (Degussa Co., Ltd., Germany) was used a benchmark (reference) photocatalyst.

**Catalytic Performance Evaluation.** To evaluate the catalytic activity, 10 mL ($1.0 \times 10^{-4}$ M) of aqueous solution of 4-nitrophenol, 0.0075 g of each of the samples were separately added followed by addition of 5 mL ($6.0 \times 10^{-2}$ M) of aqueous $NaBH_4$ solution to the reaction mixture under ice-cold conditions and time-dependent absorption spectra were recorded.

**Photoanode Preparation.** To prepare the photoanodes, we mixed mechanically excess quantities of the composites with a commercial $TiO_2$ paste (Man Solar) in the weight ratio of 9:1. The commercial $TiO_2$ paste contained a transparent conducting polymer and a binding agent which help in improving the film quality and stability. After having coated them on ITO glass surfaces (surface resistivity R = 28 – 30 Ω $cm^{-2}$), the films were heated at 350 ºC for 40 min. Commercial carbon paste (R = 110 – 120 Ω $cm^{-2}$) coated on ITO surfaces is used as the cathode. Natural flavonoid anthocyanin dye extracted from hibiscus flower, which can absorb visible light in the range of 475–650 nm wavelength with the characteristic absorption peak $\lambda_{max}$ at 540 nm, are directly used as sensitizer. The $I^-_3/I^-$ couple in acetonitrile is used as the electrolyte. The photoanodes' active areas were about 6 $cm^2$. The active area of illumination was maintained at 1000 ± 10 $Wm^{-2}$ (using PL-110SM Voltcraft, solar radiation measuring instrument, Conrad Electronics SE Hirschau) with an artificial indoor lamp. The power conversion efficiency of the DSSC (η) is the product of three terms: the short circuit photocurrent density ($J_{SC}$), the open-circuit photovoltage ($V_{OC}$) and the fill factor (FF) divided by the incoming incident solar power ($P_{in}$). The η values are evaluated according to Equation (6):

$$\eta = (J_{SC} \times V_{OC} \times FF) / P_{in} \quad (7)$$

The FF value is defined as ratios of maximum power output ($J_{max} \times V_{max}$) and the product of Jsc and Voc.

$$FF = (J_{max} \times V_{max}) / (J_{SC} \times V_{OC}) \quad (8)$$

Maximizing any of the numerator terms in Equation (6) will increase η. From the cross-sectional SEM images, the thickness of the films prepared from the composite materials is verified to be about 12±2 μm.

## *Acknowledgements*

*TS thanks the Alexander von Humboldt Foundation, Bonn, Germany for a postdoctoral fellowship and research grants. We also thank Dr. Kallol Ray, Junior Research Group Leader at the Humboldt-University, Berlin, within the Uni-Cat cluster of excellence for his support with the photocatalytic experimental set-up and Dr. Gregor Meier, Inorganic Chemistry and Homogeneous Catalysis Group, Humboldt-University, Berlin for his help with FT-IR measurements.*

**Keywords:** Graphene Oxide • Composite Materials • Photocatalysis • Photovoltaic Devices • Catalysis

[1] Q. Xiang, J. Yu, M. Jaroniec, *Chem. Soc. Rev.* **2012**, *41*, 782–796.

[2] W. Tu, Y. Zhou, Z. Zou, *Adv. Func. Mater*. **2013**, DOI: 10.1002/adfm.201203547.

[3] J. Liu, H. Bai, Y. Wang, Z. Liu, X. Zhang, D. D. Sun, *Adv. Func. Mater*. **2010**, *20*, 4175–4181.

[4] J. Tian, H. Li, A. M. Asiri, A. O. Al-Youbi, X. Sun, *Small* **2013**, *9*, 2709–2714.

[5] H. Yang , Y. Kwon , T. Kwon , H. Lee , B. J. Kim, *Small* **2012**, *8*, 3161–3168.

[6] C. Huang, C. Li, G. Shi, *Energy Environ. Sci*. **2012**, *5*, 8848–8868.

[7] Q. Xiang, J. Yu, M. Jaroniec, *Nanoscale* **2011**, *3*, 3670-3678.

[8] Q. Xiang, J. Yu, J. *Phys. Chem. Lett*. **2013**, *4*, 753−759.

[9] Q. Xiang, J. Yu, M. Jaroniec, *J. Am. Chem. Soc*. **2012**, *134*, 6575−6578.

[10] H. –X. Wang, Q. Wang, K. -G. Zhou, H. –L. Zhang, *Small* **2013**, *9*, 1266–1283.

[11] J. Liu, Y. Xue, Y. Gao, D. Yu, M. Durstock, L. Dai, *Adv. Mater.* **2012**, *24*, 2228–2233.

[12] N. G. Sahoo, Y. Pan, L. Li, S. H. Chan, *Adv. Mater.* **2012**, 24, 4203–4210.

[13] B. Li, T. Liu, Y. Wang, Z. Wang, *J. Colloid Inter. Sci.* **2012**, *377*, 114–121.

[14] C. Chen, W. Cai, M. Long, B. Zhou, Y. Wu, D. Wu, Y. Feng, *ACS Nano* **2010**, *4*, 6425–6432.

[15] W. Wang, J. Yu, Q. Xiang, B. Cheng, *Appl. Cat. B* **2012**, *119-120*, 109-116.

[16] T. Wu, J. Ma, X. Wang, Y. Liu, H. Xu, J. Gao, W. Wang, Y. Liu, J. Yan, *Nanotech*. **2013**, 24, 125301.

[17] M. Jahan, Z. Liu, K. P. Loh," A Graphene Oxide and Copper-Centered Metal Organic Framework Composite as a Tri-Functional Catalyst for HER, OER, and ORR," Adv. Func. Mater. 2013 DOI: 10.1002/adfm.201300510.

[18] Z. Yin, S. Wu, X. Zhou, X. Huang, Q. Zhang, F. Boey, H. Zhang, *Small* **2010**, *6*, 307–312.

[19] D. Chen, H. Feng, J. Li, *Chem. Rev*. **2012**, *112*, 6027−6053.

[20] D. R. Dreyer, S. Park, C. W. Bielawski, R. S. Ruoff, *Chem. Soc. Rev*. **2010**, *39*, 228–240.

[21] S. Park, R. S. Ruoff, *Nature Nanotech*. **2009**, *4*, 217–224.

[22] K. P. Loh, Q. Bao, G. Eda, M. Chhowalla, *Nature Chem*. **2010**, *2*, 1015-1024.

[23] G. Eda, G. Fanchini, M. Chhowalla, *Nat. Nanotechnol*. **2008**, *3*, 270-274.

[24] S. Pei, H. –M. Cheng, *Carbon* **2012**, *50*, 3210-3228.

[25] P. V. Kamat, *J. Phys. Chem. Lett.* **2011**, *2*, 242–251.

[26] M. J. McAllister, J.-L. Li, D. H. Adamson, H. C. Schniepp, A. A. Abdala, J. Liu, M. Herrera-Alonso, D. L. Milius, R. Car, R. K. Prud'homme, I. A. Aksay, *Chem. Mater*. **2007**, *19*, 4396–4404.

[27] A. Mathkar, D. Tozier, P. Cox, P. Ong, C. Galande, K. Balakrishnan, A. L. M. Reddy, P. M. Ajayan, *J. Phys. Chem. Lett.* **2012**, *3*, 986−991.

[28] S. Kim, S. Zhou, Y. Hu, M. Acik, Y. J. Chabal, C. Berger, W. de Heer, A. Bongiorno, E. Riedo, *Nature Mater*. **2012**, *11*, 544-549.

[29] I. V. Lightcap, S. Murphy, T. Schumer, P. V. Kamat, *Phys. Chem. Lett.* **2012**, *3*, 1453−1458.

[30] X. Zuo, S. He, D. Li, C. Peng, Q. Huang, S. Song, C. Fan, *Langmuir* **2010**, *26*, 1936−1939.

[31] M. Jin, H. –K. Jeong, W. J. Yu, D. J. Bae, B. R. Kang, Y. H. Lee, *J. Phys. D. Appl. Phys.* **2009**, *42*, 135109.

[32] Y. Zhu, S. Murali, W. Cai, X. Li , J. W. Suk , J. R. Potts, R. S. Ruoff, *Adv. Mater.* **2010**, *22*, 3906–3924.

[33] X. Wu, M. Sprinkle, X. Li, F. Ming, C. Berger, W. A. de Heer, *Phys. Rev. Lett.* **2008**, *101*, 026801.

[34] S. Gilje, S. Han, M. Wang, K. L. Wang, R. B. Kaner, *Nano Lett.* **2007**, *7*, 3394−3398.

[35] O. C. Compton, S. T. Nguyen, *Small* **2010**, *6*, 711−723.

[36] C. Yu, W. Ji, Y. Wang, N. Bao, H. Gu, *Nanotechnology* **2013**, *24*, 115502.

[37] J. D. Roy-Mayhew, G. Boschloo, A. Hagfeldt, I. A. Aksay, *ACS Appl. Mater. Inter.* **2012**, *4*, 2794−2800.

[38] H. Wang, Y. H. Hu, *J. Colloid Inter. Sci.* **2013**, *391*, 21–27.

[39] O. O. Kapitanova, G. N. Panin, A. N. Baranov, T. W. Kang, *J. Korean Phys. Soc.* **2012**, *60*, 1789-1793.

[40] P. Madhusudan, J. Yu, W. Wang, B. Chenga, G. Liu, *Dalton Trans*. **2012**, *41*, 14345–14353.

[41] F. Dong, Y. Sun, M. Fu, W. –K. Ho, S. C. Lee, Z. Wu, *Langmuir* **2012**, 28, 766–773.

[42] F. Amano, K. Nogami, M. Tanaka, B. Ohtani, *Langmuir* **2010**, 26, 7174–7180.

[43] Huo, Y. N.; Miao, M.; Zhang, Y.; Zhu, J.; Li, H. X. Chem. Commun. 2011, 47, 2089–2091

[44] L. Zhang, C. Baumanis, L. Robben, T. Kandiel, D. Bahnemann, *Small* **2011**, *7*, 2714–2720.

[45] M. D. Hernández-Alonso, F. Fresno, Silvia Suárez, J. M. Coronado, *Energy Environ. Sci*. **2009**, *2*, 1231–1257.

[46] T. Saison, N. Chemin, C. Chanéac, O. Durupthy, V. Ruaux, L. Mariey, F. Maugé, P. Beaunier, J.-P. Jolivet, *J. Phys. Chem. C* **2011**, *115*, 5657–5666.

[47] S. G. Kumar, L. G. Devi, *J. Phys. Chem. A*, **2011**, *115*, 13211–13241.

[48] P. K. Panda, *J. Mater. Sci.* **2009**, *44*, 5049–5062.

[49] S. Taufik, N. A. Yusof, T. W. Tee, I. Ramli, *Int. J. Electrochem. Sci.* **2011**, *6*, 1880 – 1891.

[50] J. Eberl, H. Kisch, *Photochem. Photobiol. Sci*. **2008**, *7*, 1400–1406.

[51] Y. Qiu, M. Yang, H. Fan, Y. Zuo, Y. Shao, Y. Xu, X. Yang, S. Yang, *CrystEngComm*, **2011**, *13*, 1843–1850.

[52] S. Anandan, G.-J. Lee, P.-K. Chen, C. Fan, J. J. Wu, *Ind. Eng. Chem. Res*. **2010**, *49*, 9729−9737.

[53] H.-Y. Jiang, K. Cheng, J. Lin, *Phys. Chem. Chem. Phys*. **2012**, *14*, 12114–12121.

[54] G. Zhu, W. Que, J. Zhang, *J. Alloys Comp*. **2011**, *509*, 9479– 9486.

[55] R. Li, W. Chen, H. Kobayashi, C. Ma, *Green Chem.* **2010**, *12*, 212−215.

[56] W. Hou, S. B. Cronin, Adv. *Funct. Mater.* **2013**, *23*, 1612–1619.

[57] S. Linic, P. Christopher, D. B. Ingram, *Nature Mater.* **2011**, *10*, 911−921.

[58] P. Wang, B. Huang, Y. Daia, M. –H. Whangbo, *Phys. Chem. Chem. Phys*. **2012**, *14*, 9813–9825.

[59] Y. Xu, H. Xu, J. Yan, H. Li, L. Huang, Q. Zhang, C. Huang, H. Wan, *Phys. Chem. Chem. Phys.,* **2013**, *15*, 5821−5830.

[60] K. Awazu, M. Fujimaki, C. Rockstuhl, J. Tominaga, H. Murakami, Y. Ohki, N. Yoshida, T. Watanabe, *J. Am. Chem. Soc.* **2008**, *130*, 1676−1680.

[61] H. –W. Wang, Z. –A. Hu, Y. –Q. Chang, Y. –L. Chen, Z. –Q. Lei, Z. –Y. Zhang, Y. –Y. Yang, *Electrochimica Acta* **2010**, *55*, 8974–8980.

[62] D. Chen, Rachel A. Caruso, *Adv. Funct. Mater*. **2013**, 23, 1356–1374.

[63] Y. Liu, Z. Wang, B. Huang, K. Yang, X. Zhang, X. Qin and Y. Dai, *Appl. Surf. Sci*., 2010, **257**, 172–175.

[64] J. Liu, H. Cao, J. Xiong, Z. Cheng, *CrystEngComm* **2012**, *14*, 5140–5144.

[65] A. K. Manna, S. K. Pati, *Chem.–Asian J.* **2009**, *4*, 855–860.

[66] E. Gao, W. Wang, M. Shang, J. Xu, *Phys. Chem. Chem. Phys.* **2011**, *13*, 2887–2893.

[67] T. Som, A. Simo, R. Fenger, G. V. Troppenz, R. Bansen, N. Pfänder, F. Emmerling, J. Rappich, T. Boeck, Klaus Rademann, *ChemPhysChem* **2012**, *13*, 2162-2169.

[68] B. Das, R. Voggu, C. S. Rout, C. N. R. Rao, *Chem. Commun*. **2008**, 5155–5157.

[69] A. K. Manna, S. K. Pati, *Chem.–Asian J.* **2009**, *4*, 855–860.

[70] R. Voggu, B. Das, C. S. Rout, C. N. R. Rao, *J. Phys. Condens. Mater* **2008**, *20*, 472204−472209.

[71] T. Wu, H. Shen, L. Sun, B. Cheng, B. Liu, J. Shen, *ACS Appl. Mater. Interfaces* **2012**, *4*, 2041−2047.

[72] C. Li, J. Zhang, K. Liu, *Int. J. Electrochem. Sci.* **2012**, *7*, 5028−5034.

[73] I.K. Konstantinou, T.A. Albanis, *Applied Catalysis B* **2004**, *49*, 1−14.

[74] H. Nishiyama, H. Kobayashi, Y. Inoue, *ChemSusChem* **2011**, *4*, 208−215.

[75] G. Li, D. Zhang, Ji. C. Yu, *Chem. Mater*. **2008**, *20*, 3983−3992.

[76] S. Tokunaga, H. Kato, A. Kudo, *Chem. Mater.* **2001**, *13,* 4624−4628.

[77] T. Hirakawa, P. V. Kamat, *J. Am. Chem. Soc*. **2005**, *127*, 3928−3934.

[78] R. Li, W. Chen, H. Kobayashi, C. Ma, *Green Chem*., **2010**, *12*, 212−215.

[79] T.-F. Yeh, F.-F. Chan, C.-T. Hsieh, H. Teng, *J. Phys. Chem. C* **2011**, *115*, 22587−22597.

[80] C.-H. Chang, X. Fan, L. -J. Li, J. –L. Kuo, *J. Phys. Chem. C* **2012**, *116*, 13788−13794.

[81] R. Sitko, E. Turek, B. Zawisza, E. Malicka, E. Talik, J. Heimann, A. Gagor, B. Feist, R. Wrzalik, *Dalton Trans.* **2013**, *42*, 5682−5689.

[82] S. Krishnamurthy, I. V. Lightcap, P. V. Kamat, *J. Photochem. Photobio. A* **2011**, *221*, 214−219.

[83] A. Wojcik, P. V. Kamat, *ACS Nano* **2010**, *4*, 6697−6706.

[84] A. Du, Y. Ng, N. J. Bell, Z. Zhu, R. Amal, S. C. Smith, *J. Phys. Chem. Lett.* **2011**, *2*, 894−899.

[85] K. Woan, G. Pyrgiotakis, W. Sigmund, Adv. *Mater*. **2009**, *21*, 2233−2239.

[86] Y. Xu, H. Xu, J. Yan, H. Li, L. Huang, Q. Zhang, C. Huang, H. Wan, Phys. *Chem. Chem. Phys*. **2013**, *15*, 5821−5830.

[87] Y. Xu, H. Bai, G. Lu, C. Li, G. Shi, *J. Am. Chem. Soc*. **2008**, *130*, 5856-5857.

[88] L. Huang, G. Li, T. Yan, J. Zheng, L. Li, *New J. Chem*. **2011**, *35*, 197–203.

[89] W. Li, Mater. *Chem. Phys*. **2006**, 99, 174–180.

[90] F. Dong, W. –K. Ho, S. C. Lee, Z. Wu, M. Fu, S. Zou, Yu Huang, *J. Mater. Chem*. **2011**, *21*, 12428.

[91] Y. Yang, Z. Cao, Y. Jiang, L. Liu, Y. Sun, Mater. Sci. Eng. B **2006**, *132*, 311–314.

[92] J. Z. Marinho, R. A. B. Silva, Tatielli G. G. Barbosa, E. M. Richter, R. A. A. MuÇoz, R. C. Lima, Electroanalysis 2013, 25, 765 – 770.

[93] P. Hervés, M. Pérez-Lorenzo, L. M. Liz-Marzán, J. Dzubiella, Y. Lub, M. Ballauff, *Chem. Soc. Rev.* **2012**, *41*, 5577−5587.

[94] G. W. Batchelder, L. C. Hurd, *J. Chem. Educ.* **1932**, *9*, 929−930.

[95] W. Lu, R. Ning, X. Qin, Y. Zhang, G. Chang, S. Liu, Y. Luo, X. Sun, *J. Hazard. Mater.* 2011, *197*, 320−326.

[96] J. Huang, L. Zhang, B. Chen, N. Ji, F. Chen, Y. Zhang, Z. Zhang, *Nanoscale* **2010**, *2*, 2733−2738.

[97] B. E. Hardin, H. J. Snaith, M. D. McGehee, *Nature Photonics* **2012**, *6*, 162−169.

[98] J. W. Bullard, M. J. Cima, *Langmuir* **2006**, *22,* 10264−10271.

[99] Ching-Hung Weng and Wen-Cheng J. Wei, *J. Am. Ceram. Soc*. **2010,** *93*, 3124−3129.

[100] A. Annamalai, Y. D. Ei, M. J. Lee, *Materials Characterization* **2011**, *62*, 1007−1015.

[101] G. Venugopal, K. Krishnamoorthy, R. Mohan, Sang-Jae Kim, *Mater. Chem. Phys.* 2012, 132, 29−33.

[102] M. Tsukamoto, N. Abe, Y. Soga, M. Yoshida, H. Nakano, M. Fujita, J. Akedo, *Appl Phys A* **2008**, *93*, 193−196.

[103] V. V. Killedar, C. H. Bhosale, C. D. Lokhande, *Turkish J. of Phys.* **1998**, *22*, 825−830.

[104] B. O. Aduda, P. Ravirajan, K. L. Choy, J. Nelson, *International Journal of Photoenergy* **2004**, *6*, 141−147.

[105] N. Robertson, *Angew. Chemie Inter. Ed.* **2006**, *45*, 2338−2345.

[106] H. Liu, L. Zhang, Y. Guo, C. Cheng, L. Yang, L. Jiang, G. Yu, W. Hu, Y. Liu, D. Zhu, *J. Mater. Chem. C* **2013**, *1*, 3104−3109.

[107] Y. H. Hu, H. Wang, B. Hu, *ChemSusChem* **2010**, *3*, 782-796.

[108] Z. Zou, J. Ye, K. Sayama, H. Arakawa, *J. Photochem. Photobio. A* **2002**, *14***8**, 65–69.

Received: ((will be filled in by the editorial staff))
Published online: ((will be filled in by the editorial staff))

ChemSusChem
Full Papers

**Entry for the Table of Contents**

Layout 1:

# FULL PAPER

Graphene Oxide (GO)/α-$Bi_2O_3$ multifunctional composite, with only 1wt% GO, exhibits ~4-6 times enhanced photocatalytic activities as compared to commercial $TiO_2$-P25 in organic dye degradation. It is also extremely useful in constructing photoanodes in dye-sensitized solar cells (DSSC) and catalyses selectively nitro to amino conversions

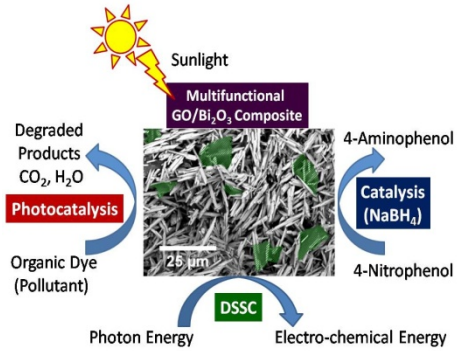


*Tirtha Som,* Gerald V. Troppenz, Robert Wendt, Markus Wollgarten, Jörg Rappich, Franziska Emmerling, Klaus Rademann*

***Page No. – Page No.***

**Title**

ChemSusChem
Full Papers
www.chemsuschem.org

## Supplementary Information

# Graphene Oxide (GO)/α-$Bi_2O_3$ Versatile Multifunctional Composites for Enhanced Visible Light Photocatalysis, Chemical Catalysis and Solar Energy Conversion

*Tirtha Som,* Gerald V. Troppenz, Robert Wendt, Markus Wollgarten Jörg Rappich, Franziska Emmerling, Klaus Rademann*

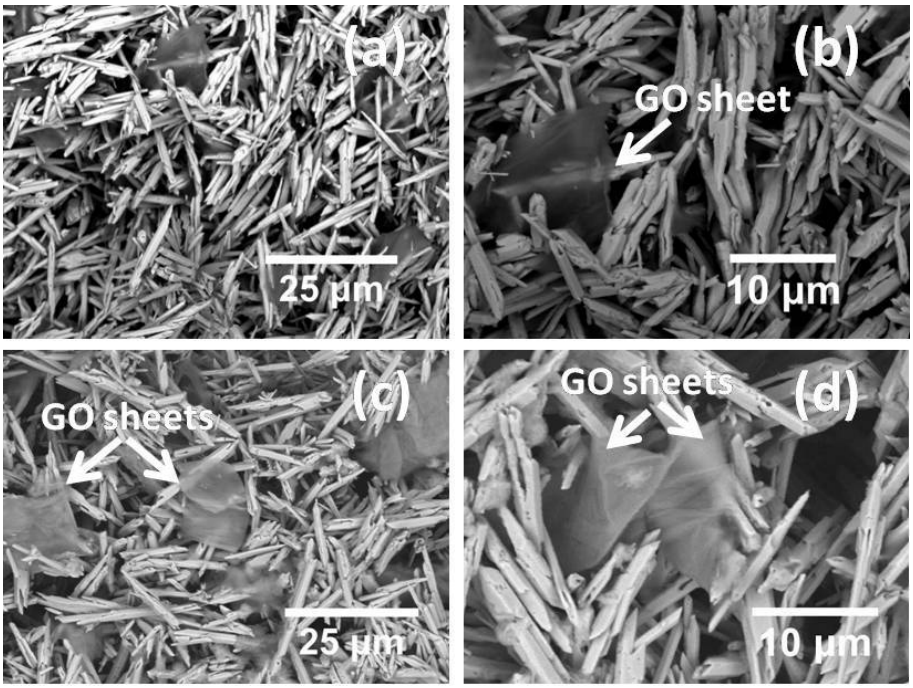


**Figure S1.** SEM images of (a) GO/$Bi_2O_3$, (b) GO/$Bi_2O_3$ at a higher magnification, (c) Ag/GO/$Bi_2O_3$ and (d) Ag/GO/$Bi_2O_3$ at a higher magnification. There are the original SEM images corresponding to **Figure 1(c-f)** in the manuscript.

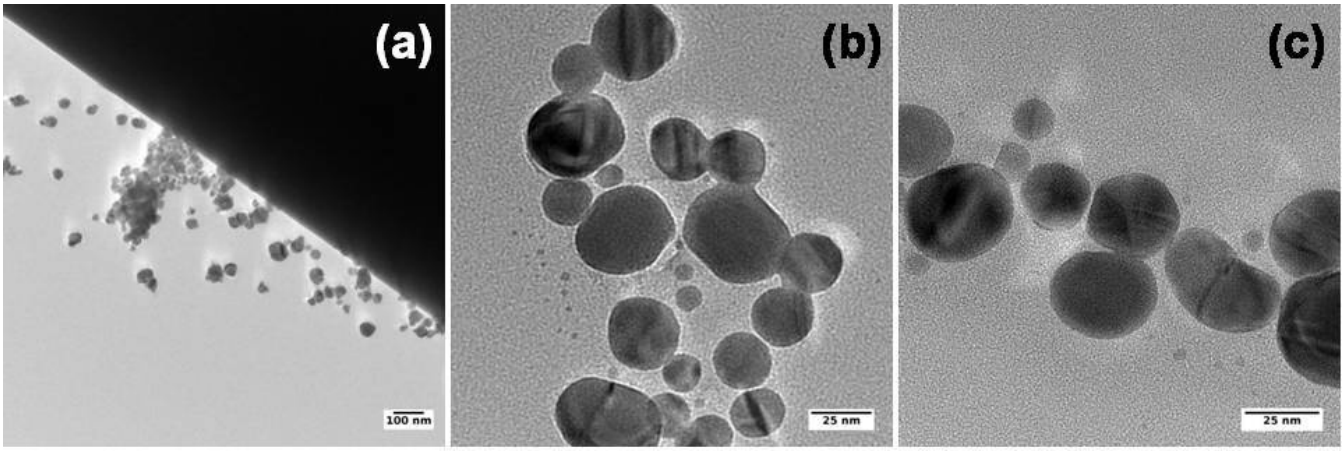


**Figure S2.** TEM images of the Ag/GO/$Bi_2O_3$ composite, showing near-spherical Ag NPs located near $Bi_2O_3$ micro-needle. Larger scale bars necessary

**Figure S3.** X-ray diffraction pattern of Ag/GO/$Bi_2O_3$.

**Figure S4.** Raman spectrum of α-$Bi_2O_3$.

**Figure S5.** Time-dependent absorption spectra of (a) Crystal Violet ($10^{-5}$ M) and (b) Rhodamine 6G ($10^{-5}$ M) solutions under simulated sunlight (visible) irradiation showing photocatalytic degradation in the presence of GO/$Bi_2O_3$ composite photocatalyst.

**Band Gap Determination for Graphene Oxide**

The Tauc plot method [S1] is used to determine the band gap ($E_g$) of the synthesized GO (**Figure S5**). For this, the UV-Vis absorption spectrum of the GO colloidal suspension is measured (**Figure S5, inset**). One absorption maximum is observed at about 245 nm due to $\pi \rightarrow \pi^*$ transition of aromatic C=C bonds.[S2,S3] A shoulder is seen at 312 nm corresponding to the $n \rightarrow \pi^*$ transition of the C=O bond in $sp^3$ hybrid domains.[S2,S3] Since GO is made of graphene molecules of varying oxidation levels, it does not show a sharp absorption edge for precise band edge determination.

The energies for the direct and indirect gap transitions are estimated by plotting the square and square root of the absorption energy (αE, where α is the absorbance) against the photon energy (E).[S1,S3,S4] The linear extrapolation of the curves in **Figures S5(a-b)** reveal that the apparent energies for the direct and indirect transition for our GO is in the range of 3.3–4.2 and 1.8–3.0 eV, respectively. This evaluated lower limit of the band-gap energies is implemented in **Figure 5** in the main text to construct the energy level diagram of GO. Literature reveals that GO with a band gap around 1.7 eV has been shown to display p-type semiconducting characteristics under ambient conditions while the GO with a band gap greater than 2.1 eV exhibits insulating behaviour. [S5]

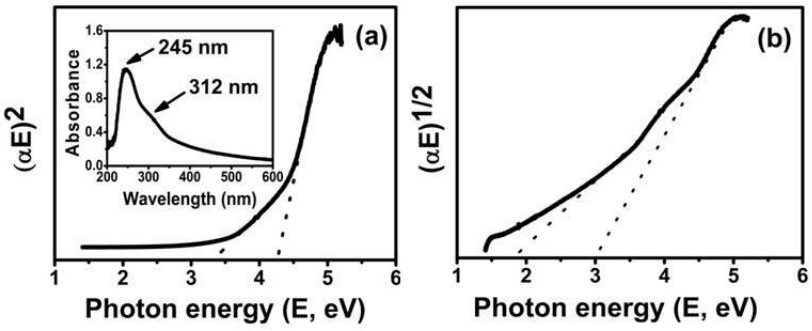


**Figure S6.** Tauc plots of (a) $(\alpha E)^2$ against the photon energy (E) for direct transition in GO and of (b) $(\alpha E)^{1/2}$ vs (E) for indirect transition in GO. Extrapolation of the plots (see dotted lines) gives the ranges of the direct and indirect band gap energies in case of GO. Inset in (a) shows the absorption spectrum of GO.

**Figure S7.** The time dependent absorption spectra for the catalytic reduction of 4-NP by $NaBH_4$ in presence of $GO/Bi_2O_3$ catalyst.

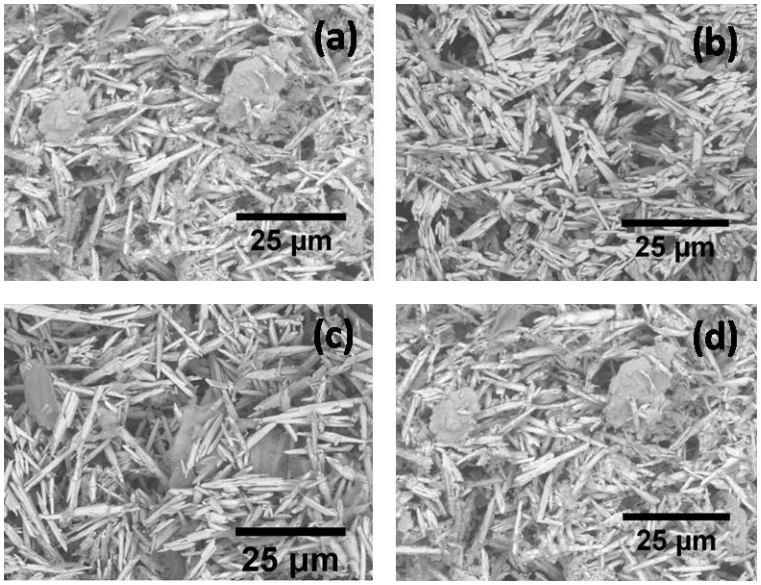


**Figure S8.** SEM images of the catalysts recovered after catalytic reduction reactions of 4-NP by NaBH4. (a) α-$Bi_2O_3$ needles reduced to metallic $Bi^0$ needles, (b) Ag-uploaded α-$Bi_2O_3$ needles reduced to $Ag^0/Bi^0$needles (c) GO/$Bi_2O_3$ transformed to reduced graphene oxide (RGO)/$Bi^0$ composite (d) Ag-uploaded α-$Bi_2O_3$ hybridized with GO reduced to $Ag^0$/RGO/$Bi^0$

## References

[S1] J. Tauc, R. Grigorovici, A. Vancu, *Phys. Status Solidi*, **1966**, *15*, 627-63.

[S2] K. P. Loh, Q. Bao, G. Eda, M. Chhowalla, *Nature Chem.*, **2010**, *2*, 1015-1024.

[S3] T.-F. Yeh, J.-M. Syu, C. Cheng, T.-H. Chang, H. Teng, *Adv. Funct. Mater.*, **2010**, *20*, 2255.

[S4] J. Liu, H. Cao, J. Xiong, Z. Cheng, *CrystEngComm*, **2012**, *14*, 5140–5144.

[S5] M. Jin, H. –K. Jeong, W. J. Yu, D. J. Bae, B. R. Kang, Y. H. Lee, *J. Phys. D. Appl. Phys.*, **2009**, *42*, 135109.